RSC Advances

PAPER

View Article Online
View Journal | View Issue

Cite this: *RSC Adv.*, 2017, **7**, 9914

$CuZrO_3$ nanoparticles catalyst in aerobic oxidation of vanillyl alcohol

Subrata Saha and Sharifah Bee Abd Hamid*

A highly crystalline, mesoporous and perovskite type $CuZrO_3$ nanoparticles catalyst was prepared *via* a simple and facile one pot solvent evaporation method. The crystal planes (112) and (211) of $CuZrO_3$ were evidenced in HRTEM and SAED imagery by their lattice parameters, 2.83 and 3.15 Å. Also, the crystallite size of synthesized catalyst was measured in a range of 7–10 nm. The catalyst was superior as it possessed many physiochemical properties to perform a liquid phase aerobic oxidation of vanillyl alcohol to selectively produce vanillin under base free conditions. Catalytic activity of the synthesized perovskite type $CuZrO_3$ catalyst was substantially improved by the presence of surface oxygen vacancies speculated in O 1s spectra. Furthermore, a O_2-TPD technique was applied to understand the role of surface oxygen vacancy in enhancing catalytic activity. Moreover, numerous partial and full lattice dislocated grain boundaries were observed as a form of structural defects between different planes in HRTEM imagery. The redox capability of this superior catalyst was significantly enriched by the high content of Zr loading and confirmed by low temperature reduction in H_2-TPR analysis. Excellent catalytic behavior of $CuZrO_3$ (Cu:2Zr) catalyst (91% conversion and 76% selectivity to vanillin) in liquid phase aerobic oxidation was well correlated with the structural and chemical properties of the catalyst. Moreover, the catalyst was stable for four consecutive oxidation reactions without appreciable loss of catalytic activity.

Received 5th November 2016
Accepted 16th January 2017

DOI: 10.1039/c6ra26370d

www.rsc.org/advances

Introduction

Catalytic upgradation of lignocellulosic biomass is a recent great challenge due to its complexity associated with structure and recalcitrance to transformation.[1] Extensive research has been explored in past decades for valorization of carbon-based biomass constituents.[2–7] Lignin is one of the less used biomass constituents due to its polymeric complex structure which limits potential applications of it in a wide range of applications. In order to create sustainable bio refineries, it is very crucial to develop a suitable catalyst system to transform the lignin fraction of biomass into selective value added products because 30% carbon and 40% of the energy content of lignocellulosic biomass constituents are lignin.[8]

Since lignin contains a large concentration of hydroxyl groups, it is viable to oxidize or cause oxidative polymerization of targeted products with environmental friendly oxidants such as H_2O_2 or O_2. Vanillyl alcohol is often considered to be one of the model compounds representing lignin since its structure is similar to one of the building block units of lignin.[9–13] Selective oxidative products of vanillyl alcohol are important platform chemicals in pharmaceutical and perfume industries and it is also used as a food grade flavor.[14,15]

Ma *et al.* summarized the homogeneous catalysts investigated for lignin valorization.[16] Also, another group of researchers reviewed using unconventional media such as ionic liquids for lignin reactions.[17] However, using ionic liquids or homogeneous catalysts has disadvantages of product separation and low selectivity although they offer good yields. Behling outlined in detail heterogeneous catalysts up to the present for oxidizing lignin and its model compounds.[13] Numerous heterogeneous catalytic systems were investigated for such applications. Recently, Ajay jha *et al.* reported that three catalytic combinations of Co_3O_4, Mn–Co mixed oxide, and reduced graphene oxide promoted a Co–Mn catalyst for aerobic oxidation of vanillyl alcohol.[18–20] This Co_3O_4 catalyst was found to be inactive without presence of the base NaOH. Using NaOH for oxidizing the alcohol caused formation of a hydroxyl bridged catalyst leading towards catalyst deactivation and production of large scale inorganic waste. Two other catalysts showed moderate catalytic activity with 62% conversion. Mariom *et al.* reported $CoTiO_3$ catalyst using H_2O_2 resulted in catalytic activity of 66% with a 6 h reaction time.[9] Recently, Balachandra *et al.* reported preparation of nano Fe_3O_4@APTES@Ni $(OH)_2$ catalyst with 73% conversion in a 8 h reaction time.[21] Also, another group of researchers reported a carbon supported iron oxide catalyst with 86% selectivity for vanillyl alcohol oxidation.[22] Though a few catalysts showed promising catalytic activity, longer reaction times using such oxidation reactions is an unfriendly economic process. Therefore, a genuine need exists

Nanotechnology and Catalysis Research Center (NANOCAT), University of Malaya, Kuala Lumpur 50603, Malaysia. E-mail: sharifahbee@um.edu.my; Fax: +60 379676956; Tel: +60 379676959

for a catalyst with high yields under mild reaction conditions with base free reactions and a simplified synthesis protocol.

Mixed metal oxide catalysts are used with a wide range of potential applications owing to their electronic properties and unique redox properties.[23] Cooperative oxide-based catalysts showed superior catalytic activity to their counterparts with single phase. Cu-based mixed oxide catalysts showed promising catalytic activity in various oxidation reactions such as oxidation of the volatile organic compounds ethanol and toluene, plus CO oxidation[24–27] and also oxidation of lignin.[13] Perovskite structured oxides especially have been widely and effectively used in hydrogenations of hydrocarbons, and also for oxidation purposes such as CO oxidation, ammonia oxidations, and catalytic combustion.[28–36] A large number of literature references previously reported the intimate relation of defect chemistry introduced by perovskite type oxide catalysts to their catalytic activity.[37–42] Thus, catalytic activity of a perovskite structured mixed oxide catalyst was notably improved by creating a large concentration of surface defect oxygens in its structure, which benefited the oxidation process. Therefore, in this study we designed a perovskite type $CuZrO_3$ catalyst prepared *via* a one pot simple and facile solvent evaporation method. Also, to enrich the concentration of surface oxygen vacant sites in the catalyst, we introduced trifluoroacetic acid (TFA) to the synthesis protocol. Emy *et al.* reported addition of TFA in a TiO_2 lattice during calcination notably improved the concentration of surface oxygen vacancies by charge neutrality.[43] Ali Ehsan *et al.* previously reported a $CuZrO_3$–CuO composite phase on thin films.[44] Moreover, catalytic activity of the $CuZrO_3$ catalysts was tested in liquid phase oxidation of vanillyl alcohol using an environmentally benign oxygen source. To the best of our knowledge, that is the pioneer report for using a perovskite type $CuZrO_3$ catalyst to oxidize vanillyl alcohol using green oxidant air. Various characterization techniques such as TG, XRD, RAMAN, XPS, FESEM, HRTEM, SAED, H_2-TPR, and O_2-TPD were employed to examine formation of the $CuZrO_3$ phase, physiochemical and textural properties such as the phase, crystallinity, electronic state, morphology, and redox properties and their influence in the catalytic action in the vanillyl alcohol oxidation. In addition, reusability of the $CuZrO_3$ catalyst was also studied in a vanillyl alcohol aerobic oxidation.

Experimental

All chemicals were purchased from various commercial sources and used without further purification. These include copper(II) acetate monohydrate (Sigma-Aldrich, 98%) zirconium(IV) butoxide (80 wt% in 1-butanol), vanillyl alcohol (Sigma-Aldrich, 98%), vanillin (Sigma-Aldrich, 97%), vanillic acid (Sigma-Aldrich, 97%), guaiacol (Sigma-Aldrich, 98%) hydrogen peroxide (30% in H_2O) (Sigma-Aldrich solution 30% in water), and acetic acid (Merck, 96%), tetrahydrofuran (Sigma-Aldrich, 99.8%), and NaOH (Merck).

Catalyst preparation

Three different catalysts with three different ratios of Cu and Zr precursors were synthesized by following a simple one pot solution method. First, copper(II) acetate (0.79 g, 4 mmol) was dissolved in 30 mL tetrahydrofuran in a 100 mL Schenk flask. After cupper(II) acetate was completely dissolved, 1.15 g (4 mmol) of zirconium butoxide $\{Zr(dmae)_4\}$ was added dropwise followed by addition of a few drops of trifluoroacetic acid to lower the pH (<3.5). Then, the reaction mixture was kept for 4 h to complete the reaction and the color of the solution turned from blue to light blue. The solvent was removed from the reaction mixture under vacuum. The material was ground to a powder and followed by calcination at 500 °C in air at a heating rate of 2 °C min^{-1}. The prepared catalyst was labeled as catalyst A (Cu : Zr). Two other catalysts labeled as Catalyst B (Cu:2Zr) and C (2Cu:Zr) were also synthesized following a similar synthesis technique by changing the concentration of zirconium butoxide (8 mmol) and copper acetate (8 mmol) respectively, in each catalytic system. Furthermore, a catalyst with composition of (Cu:2Zr) was also prepared without addition of trifluoroacetic acid.

Characterization of $CuZrO_3$ catalyst

Thermal analysis was carried out in a ceramic crucible on a PerkinElmer TGA 4000 Thermogravimetric Analyzer connected with a computer interface. Pure air with a flow rate of 30 cm^3 min^{-1} was passed continuously at a heating rate of 10 °C min^{-1} under atmospheric pressure. The X-ray diffractograms of prepared catalysts were recorded on a D8 Advance X-ray diffraction-Bruker AXS using Cu Kα radiation (d = 1.54 Å) in range of Bragg angle 5° to 90° with a step size of 0.026/min. During the analysis, the voltage and the current density were maintained at 40 kV and 40 mA respectively, at ambient temperature. Surface morphology analysis was performed by field emission scanning microscopy (FESEM Quanta FEI 200F) and elemental composition analysis was measured by energy dispersive X-ray spectroscopy (INCA Software) attached to the FESEM. Nitrogen adsorption desorption measurements were carried out on a Micrometric ASAP 2010 instrument at −196 °C. The catalysts were first degassed at 150 °C for 5 h before analysis. Lattice spacing and selected area electron diffraction (SAED) patterns were collected using high-resolution transmission electron microscopy (HR-TEM, JEM 2100-F) at a constant voltage of 200 keV.

Temperature programmed reductions and oxidations were performed on a Micrometrics Chemisorb 1100 series instrument. Before analysis, surface moisture from 0.2 g catalyst was removed *via* pretreatment at 180 °C for 1 h by N_2 gas (20 mL min^{-1}). Then, the analysis was carried out under process conditions until 900 °C under gas flow of 5% H_2 with 95% N_2 mixtures at a heating rate of 10 °C min^{-1} and was held for 10 min. The reduced sample also was further re-oxidized to investigate the oxidation steps of the catalyst at the same temperature programme. ICP-MS analysis of the reaction mixture was performed before and after a catalytic reaction following the method ASTM-D5185 using a PerkinElmer NexION 350S series.

Catalytic activity measurement

Liquid phase aerobic oxidation was performed in a high pressure 200 mL autoclave reactor supplied by Parr Co. In a typical aerobic

oxidation reaction, 3 mmol vanillyl alcohol was dissolved in 60 mL acetonitrile with a catalyst loading of 0.0025 g cm^{-3} while the reactor temperature and pressure were kept at 120 °C and 21 bar air pressure, respectively. The oxidative products were collected by a syringe filter after every half an hour interval and analyzed by an Agilent Technology HPLC Chromatography 1100 series instrument connected to a UV detector and computer interface. A mixture of solvent (85% water + 15% acetonitrile) with 1% acetic acid was used as the mobile phase with a Zobrax RP-C18 column. The products and substrate were successfully detected by a UV detector at λ_{max} = 270 nm. The column temperature was stable at 28 °C with a flow rate of 1 mL min^{-1}.

Results and discussions

Catalyst characterizations

Thermal stability. There were two distinctive weight losses detected with TG/DTG analysis of the synthesized catalyst B (Cu:2Zr) before calcination (Fig. 1). The continuous weight loss of 13.43% with a peak maximum at 280 °C can be ascribed to loss of surface moisture and crystallite water from bulk $CuZrO_3$ catalyst. The maximum weight loss of 46.30% with peak maximum at 330 °C possibly corresponds to removal of an acetate organic group present in the metal precursors as CO_2 and water. Two minor weight losses of 1.13% and 0.56% at 440 °C and 550 °C might be due to elimination of further impurities from the catalyst. The amount of residue of 38.52% was constant until 700 °C indicating thermal stability of the catalyst at higher temperatures.

Crystal phase and crystallinity. The chemical formula and the phase were detected by XRD diffractogram analysis based on Xpert High score plus an analysis database (Fig. 2). Careful observation of the recorded XRD pattern suggests that the synthesized crystal was identified as $CuZrO_3$ phase in accordance with the JCPDS number (ICSD 00-043-0953). However, presence of a minor phase CuO was also detected which matched with the database containing Terorite (ICSD 98-002-6715). The peak positions at 2 theta = 24.33, 28.29, 31.58, 34.34, 41.01, 49.47, 50.41, 54.41, 55.56, 58.23, 60.01, and 61.72

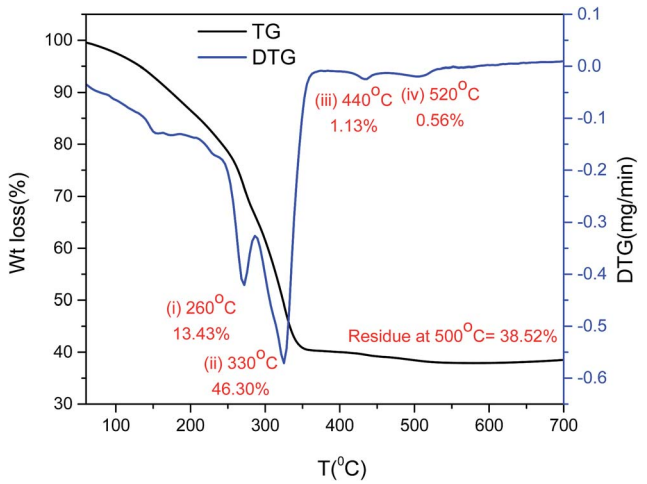

Fig. 1 Thermogravimetric analysis of synthesized catalyst B (Cu:2Zr).

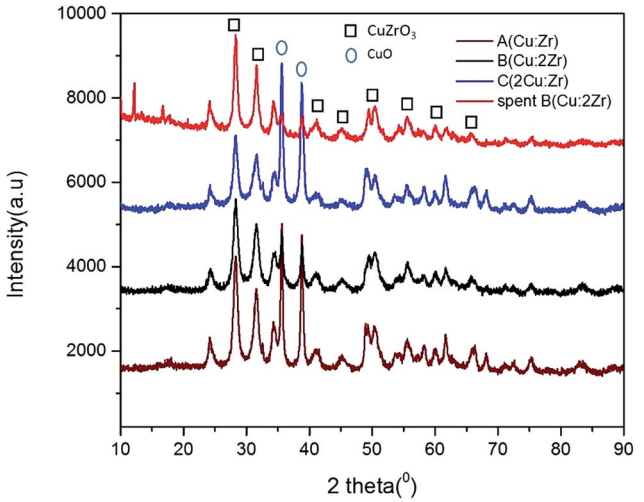

Fig. 2 The XRD pattern of catalyst A (Cu:Zr), catalyst B (Cu:2Zr), catalyst C (2Cu:Zr) and spent catalyst B (Cu:2Zr).

respectively, with d spacing (Å) 3.67, 3.15, 2.83, 2.61, 2.20, 1.84, 1.81, 1.69, 1.65, 1.58, 1.54, and 1.50 respectively, exactly correspond to miller indices (012), (112), (211), (013), (023), (040), (321), (322), (313), (401), (134), and (402) planes of $CuZrO_3$, respectively. Also, the peak positions at 2 theta = 35.61 and 38.81, respectively can be ascribed to the planes of $(11\bar{1})$ and (111) of CuO. Hence, the catalyst was synthesized as a highly crystalline perovskite shaped $CuZrO_3$ catalyst with a minor phase of CuO and with no other impurities. In addition, the orthorhombic shape having the cell parameters (a = 6.4465 Å, b = 7.4008 Å, and c = 8.3128 Å) varied from the typical cubic shape of a perovskite structure (a = 3.905 Å). This fact indicates displacement of the B cation (Zr) introducing distortions in the domain of the perovskite crystal.[45] This phenomenon would imply appreciable surface defects in the material which is one of

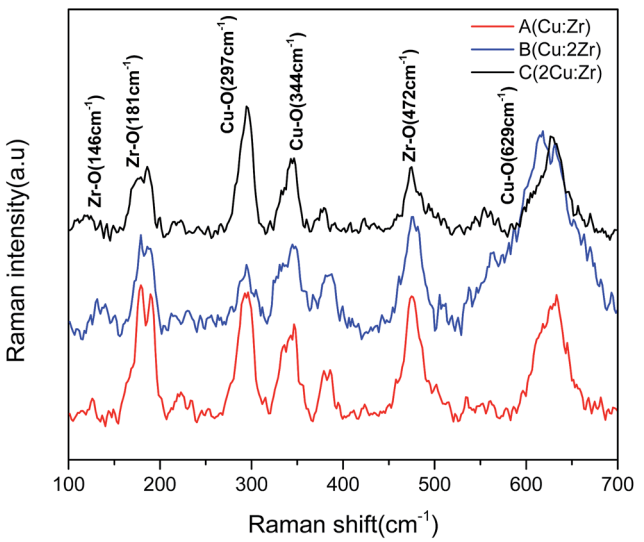

Fig. 3 Raman analysis of synthesized catalyst A (Cu:Zr), catalyst B (Cu:2Zr) and catalyst C (2Cu:Zr).

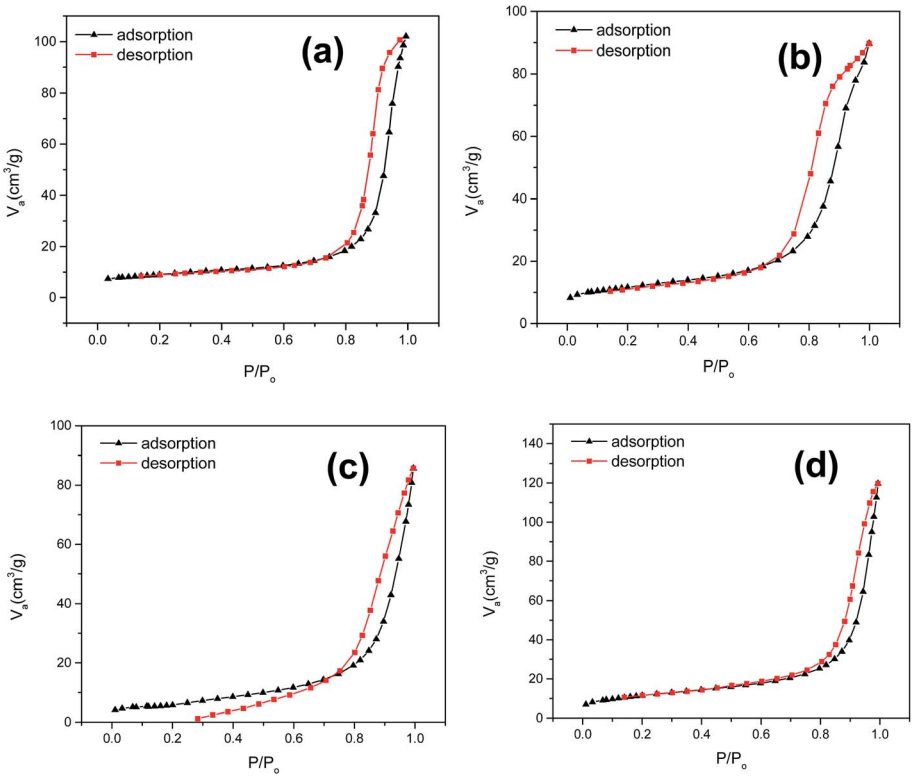

Fig. 4 N_2 adsorption–desorption curve for (a) catalyst A (Cu:Zr); (b) catalyst B (Cu:2Zr); (c) catalyst C (2Cu:Zr); (d) spent catalyst B (Cu:2Zr).

the clues to the significant catalytic activity of the perovskite type mixed $CuZrO_3$ catalyst.

The reused catalyst B (Cu:2Zr) was also characterized by XRD to detect any change in the phase, chemical composition, and crystallinity. There was no change observed in the phase and chemical composition as the recorded XRD fingerprints for spent catalyst showed the same pattern as the fresh catalyst based on peak location at Bragg angle. However, the crystallinity was slightly reduced relative to the fresh catalyst after performing the catalytic reaction.

Raman analysis. The Raman spectrum observed in Fig. 3 shows two distinctive patterns of Zr–O bonds and Cu–O bonds. Raman shift of Zr–O bonds was present at 146 cm^{-1}, 181 cm^{-1}, and 472 cm^{-1}, respectively.[46] The presence of Raman active modes of Cu–O bond was observed at 297 cm^{-1} (Ag), 344 cm^{-1} (Bg), and 629 cm^{-1} (Bg), respectively.[47] In the Raman spectrum at 616 to 635 cm^{-1}, peak shifting was observed. In bulk (Cu:2Zr) catalyst, the Raman peak was noticeably shifted to the left relative to bulk (Cu:Zr) catalyst and was attributed to the larger concentration of Zr–O bonds in the $CuZrO_3$ catalyst structure. To the contrary, the Raman peak of bulk (2Cu:Zr) catalyst with higher loading of Cu slightly shifted to the right and was attributed to the larger concentration of Cu–O bonds. It is worthwhile to mention that shorter bond lengths of Cu–O facilitates a blue Raman shift as a result of a stress and strain phenomenon.[43] Furthermore, it was noticed that a larger stoichiometric ratio of Cu in the $CuZrO_3$ catalyst (Cu:2Zr) induces structure defects and thus results in blue Raman shifting as well. In addition, the broadening of the peak illustrates structural distortion associated with the formation of the perovskite structure $CuZrO_3$.[48]

Textural property. In order to attribute textural properties of the catalysts to catalytic activity, a BET N_2 adsorption–desorption isotherm was employed (Fig. 4); it demonstrated a type (III) type isotherm and slit shaped pore distribution. One of the key barriers to obtaining high catalytic activity of a perovskite type oxide is low surface area.[49] Textural properties such as pore size, pore diameter, and BET surface area (Table 1) of a synthesized $CuZrO_3$ catalyst clearly suggest that the catalyst *via* this facile solution method has moderate surface area with mesoporosity in the structure. Also, it is worthwhile to note that higher loading of ZrO_2 in catalyst B (Cu:2Zr) contributed to enrichment of the surface area (40.83 m^2 g^{-1}) whereas it resulted in a decrement (20%) in the case of low Zr loaded catalysts A (Cu:Zr) and C (2Cu:Zr) in the bulk phase of the $CuZrO_3$ catalyst. The enrichment by 2 fold magnitude in the BET surface area of catalyst B (Cu:2Zr) was reasonably the key parameter to be

Table 1 Textural properties derived from N_2 adsorption–desorption isotherms

Catalyst	S_{BET}[a] (m^2 g^{-1})	V_t[b] (cm^3 g^{-1})	D_{BJH}[c] (nm)
A (Cu:Zr)	31.52	0.1578	20.02
B (Cu:2Zr)	40.83	0.1387	13.59
C (2Cu:Zr)	20.00	0.1325	26.49

[a] BET surface area. [b] The total pore volume. [c] BJH average pore diameter.

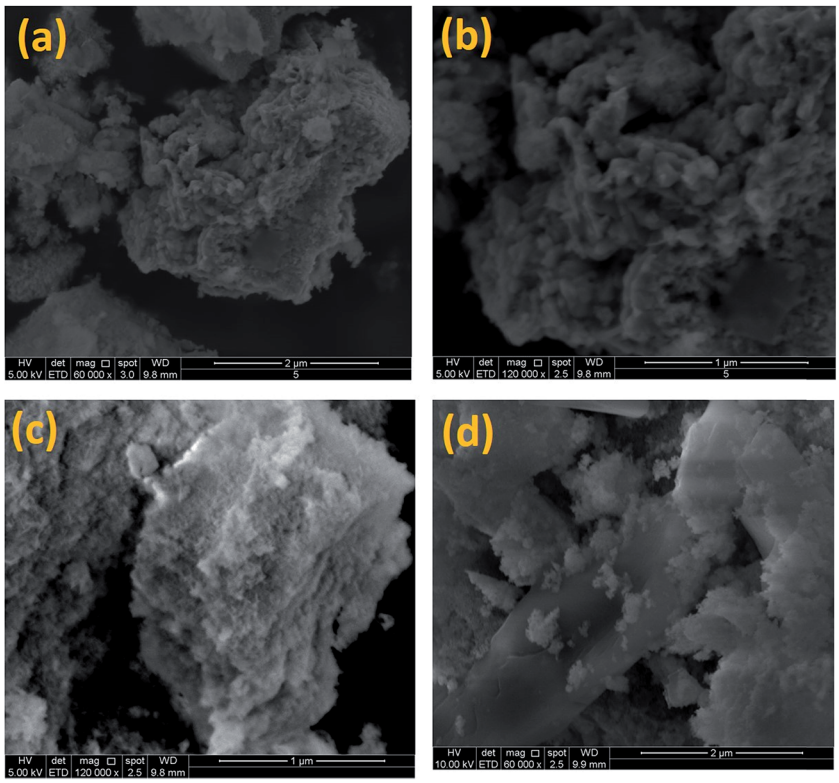

Fig. 5 Topography of $CuZrO_3$ catalysts. (a) Catalyst A (Cu:Zr); (b) catalyst B (Cu:2Zr); (c) catalyst C (2Cu:Zr); (d) spect catalyst B.

observed (Fig. 15). Moreover, it was found that textural properties of the spent catalyst remained almost unchanged after the oxidation reaction.

Morphology. Morphology of the fresh and spent catalysts was studied by FESEM under various resolutions as shown in Fig. 5. Images revealed that the catalyst is an agglomerated flakes type with a rough surface. The uneven surface is believed to perform superior catalytic activity as it facilitates chemisorption of the reactants that take part in the selective oxidation reaction of vanillyl alcohol to vanillin. However, the FESEM micrographs of the used catalyst demonstrated a plane surface which possibly indicates lower adsorption of reactants to the surface (Fig. 5d).

Furthermore, high resolution TEM equipped with SAED was used to observe presence of the $CuZrO_3$ crystal phase in terms of *d* spacing (Å) for catalyst B (Cu:2Zr) (Fig. 6). Image (Fig. 6b) of the catalyst B (Cu:2Zr) confirms the miller planes of (112) and (211) of the $CuZrO_3$ nanocrystalline domain with *d* spacing of 2.83 Å and 3.15 Å, respectively. In addition, the image shows presence of numerous grain boundaries between the lattice planes accommodated by the lattice dislocations (Fig. 6b). Grain boundaries dislocations observed in $CuZrO_3$ catalyst consist of two types: full dislocation (labelled as F) and partial dislocation (labelled as T) which lead to stalking faults (Fig. 6e).[50] It was postulated that grain boundaries in the form of surface defects can increase the catalytic activity substantially because it acts as a trapping site in the catalyst.[51–54] Moreover, the average crystallite sizes of the $CuZrO_3$ catalyst (Cu:2Zr) were measured from the observed images and determined to be in the range of 7 to 10 nm (Fig. 7c). The selective area electron diffraction pattern (SAED) was applied to further support the lattice parameters (*d* spacing) of the $CuZrO_3$ catalyst (Cu:2Zr) (Fig. 6d). Diffused rings with bright spots in the SAED pattern revealed that the catalyst was polycrystalline. In addition, the bright spots observed in the SAED pattern correspond to the plane index of (112), (211), and (013) of a $CuZrO_3$ nanocrystalline catalyst.

Additionally, the EDX spectrum of synthesized $CuZrO_3$ catalysts with different metal loadings was acquired to confirm the elemental composition (Fig. 7). The observed percentage of atomicity tentatively confirms the elemental ratio of Cu and Zr loaded in the catalyst synthesis protocol.

Oxidation state and surface analysis. Surface elemental composition and oxidation state of the synthesized $CuZrO_3$ catalyst (Cu:2Zr) were investigated using X-ray Photoelectron Spectrum (XPS) as an analytical tool (Fig. 8). The XPS wide spectrum of the catalyst further confirmed presence of Cu, Zr, and O with no other impurities of the peaks located at binding energy 933.2 eV, 181.9 eV, and 529.2 eV for Cu 3d, Zr 3d, and O 1s spin orbitals, respectively (Fig. 8a). Also, the surface elemental composition of $CuZrO_3$ (Cu:2Zr) catalyst is listed in Table 2. To obtain further information on the chemical state of the components of the catalyst, high resolution spectra of particular interesting areas were examined and shown in Fig. 8. There were two distinguishable peaks positioned at 181.81 eV and 184.18 eV attributed by doublet terms of Zr $3d_{3/2}$ and Zr $3d_{5/2}$

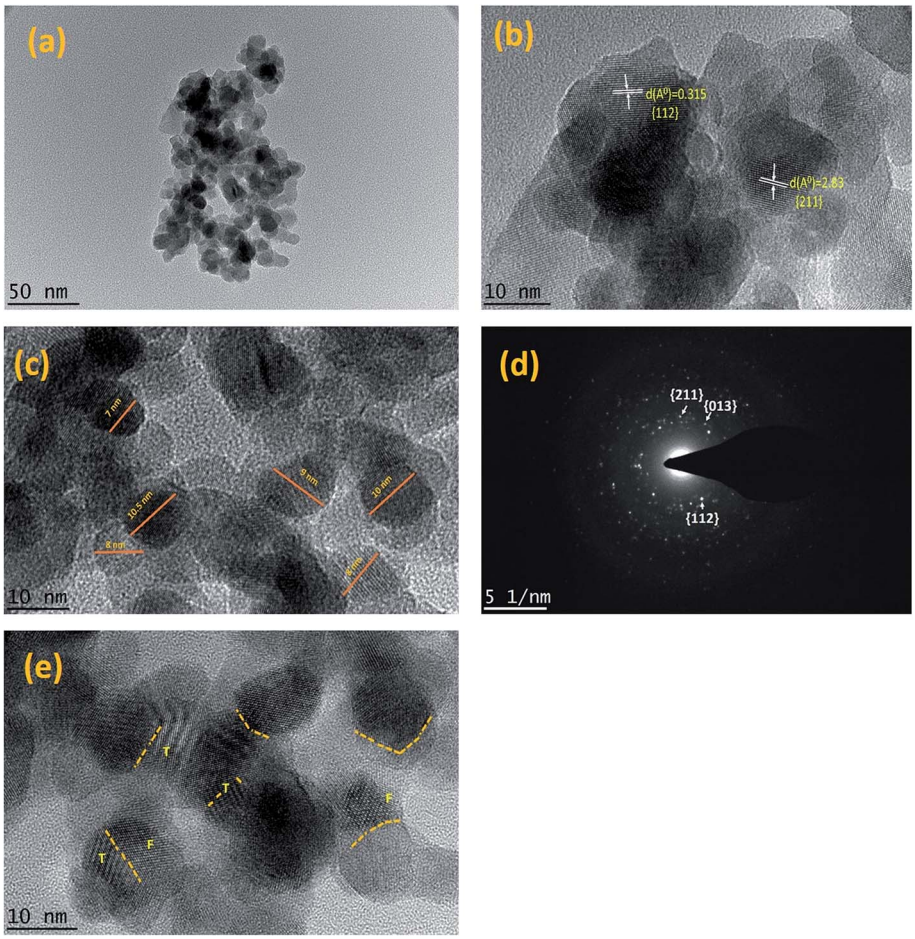

Fig. 6 HRTEM images of mixed oxide $CuZrO_3$ (Cu:2Zr) catalyst (a) overview of $CuZrO_3$ (b) measured lattice spacing. (c) Measured particle sizes. (d) SAED pattern (e) observed grain boundaries. (Full dislocation labeled as F and partial dislocation as T).

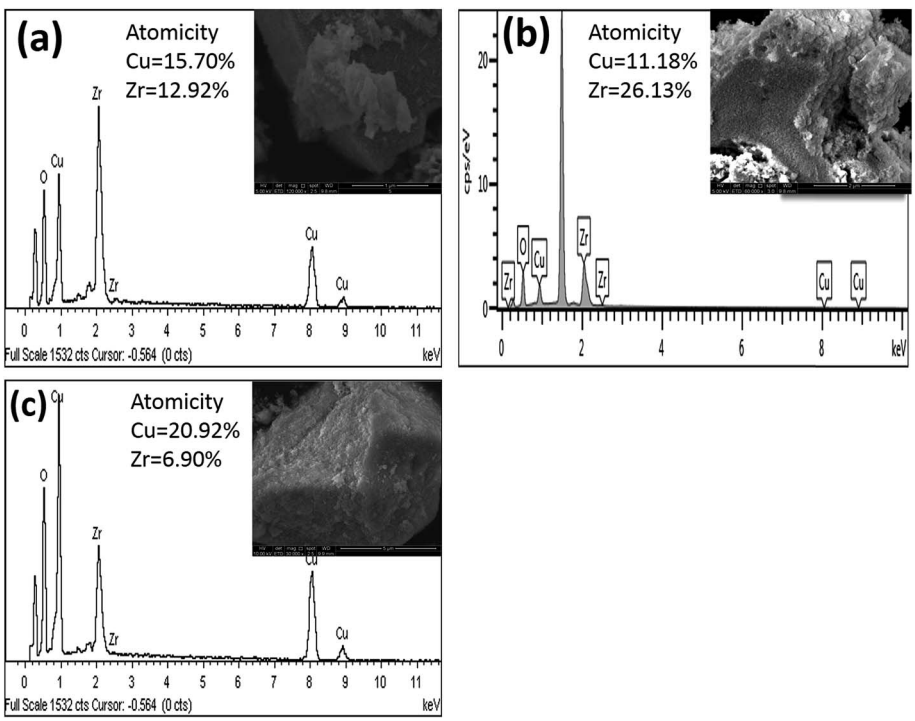

Fig. 7 EDX spectra of [a] catalyst A (Cu:Zr); [b] catalyst B (Cu:2Zr); [c] catalyst C (2Cu:Zr).

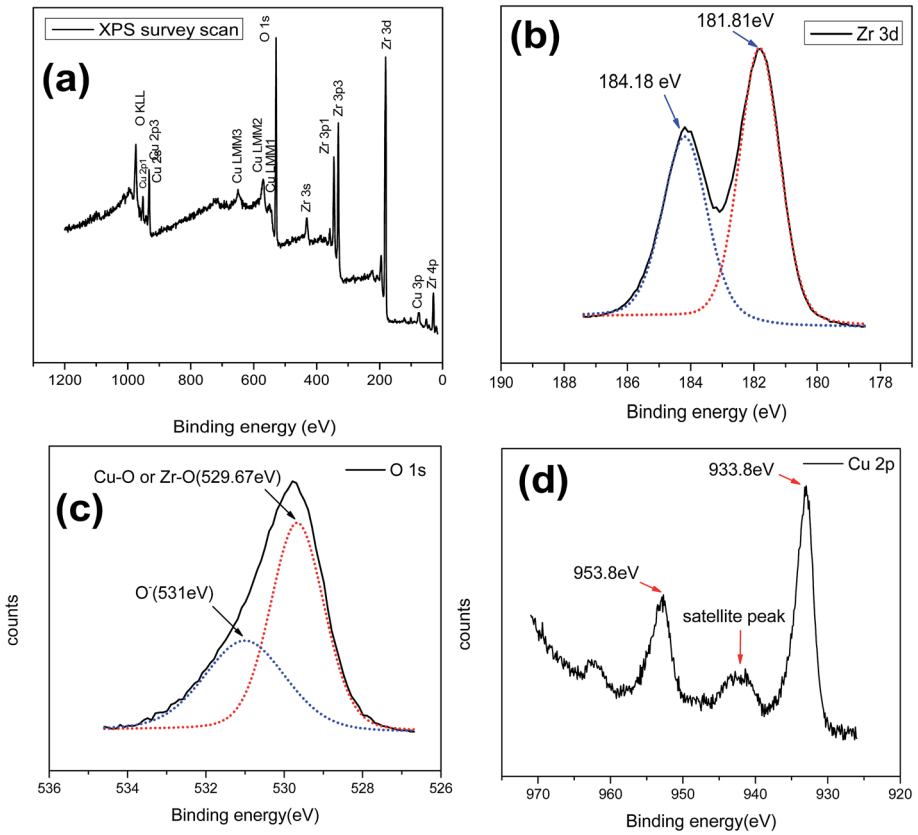

Fig. 8 XPS spectra of mixed oxide $CuZrO_3$ catalyst (Cu:2Zr). (a) Survey spectrum of $CuZrO_3$ (b) Zr 2p (c) O 1s (d) Cu 2p.

in Zr 3d spectra due to spin orbital coupling (Fig. 8b). Moreover, the energy difference between the two spin orbitals by 2.4 eV further confirms presence of the Zr^{4+} oxidation state which is in good agreement with previously reported values of ZrO_2.[55] The photoelectrons split from the spin orbital of Cu $3d_{3/2}$ and Cu $3d_{5/2}$ at 933.8 eV and 953.88 eV, respectively evidently correspond to the Cu^{2+} oxidation state (Fig. 8d).[56] Furthermore, the presence of a satellite peak in between 940–950 eV in Cu 2p spin spectra ascertained the Cu^{2+} chemical state.[57] Two peaks were observed at binding energies 529.67 eV and 531 eV in a O 1s spin orbital using nonlinear de Gaussian measurements (Fig. 8c). The peak at low binding energy 529.67 eV corresponds to the O^{2-} chemical state which represents Cu–O and Zr–O linkages present in the catalyst framework. The higher binding energy peaks at 531 eV can be attributed to weakly held oxygen species (O^-, O_2^-) at the surface compared to lattice oxygen species (O^{2-}) which is in good agreement with previously reported results by Roberts *et al.*[58] Deng *et al.* also reported presence of oxygen vacancy on the surface of a perovskite type Cu doped Co based oxide catalyst based on the higher binding energy peak of O 1s spectra in between 531 to 532 eV.[59] A similar observation was also previously reported for a La-based transitional perovskite catalyst.[41] Thus, based on similar observations in this work, the presence of oxygen vacancy in the synthesized perovskite type $CuZrO_3$ catalyst was supported. Furthermore, formation of oxygen vacancy on the catalyst surface was further triggered *via* a charge compensation phenomenon, and also during the calcination process, as a result of trifluoroacetic acid addition during the synthesis step for TiO_2.[43] A similar demonstration was observed in this $CuZrO_3$ catalyst. Moreover, the percentage of surface oxygen vacancy and lattice oxygen was calculated based on the peak area obtained in O 1s spectra (Table 3).

Table 2 Surface elemental atomicity in XPS analysis for catalyst B (Cu:2Zr)

Cu (%)	Zr (%)	O (%)
8.06	25.41	66.39

Table 3 Area percentage of oxygen species based on O 1s spectra in catalyst B (Cu:2Zr)

Lattice oxygen (%)	Surface oxygen (%)
60.30	39.70

Redox analysis. The H_2-TPR spectrum clearly revealed the reduction potential of the synthesized catalyst (Fig. 9). A careful observation of spectra in the range of 180 °C to 400 °C indicated a broad reduction peak with a shoulder peak towards a lower reduction temperature. The shoulder peak with a maximum at 200 °C could be attributed to desorption of oxygen (O^-, O_2^-)

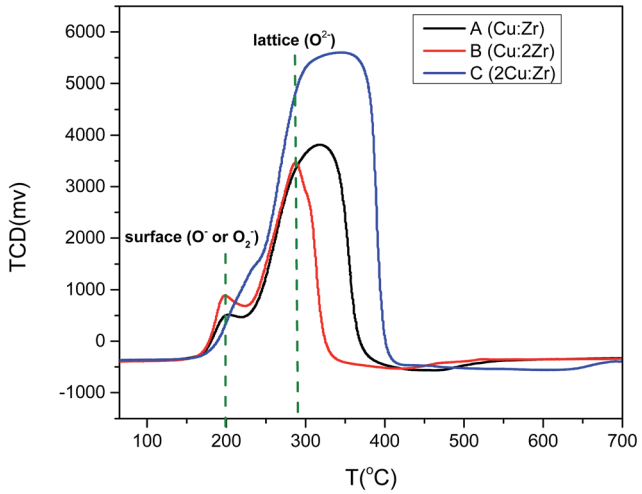

Fig. 9 H_2-TPR profile of catalyst A (Cu:Zr), catalyst B (Cu:2Zr), catalyst C (2Cu:Zr).

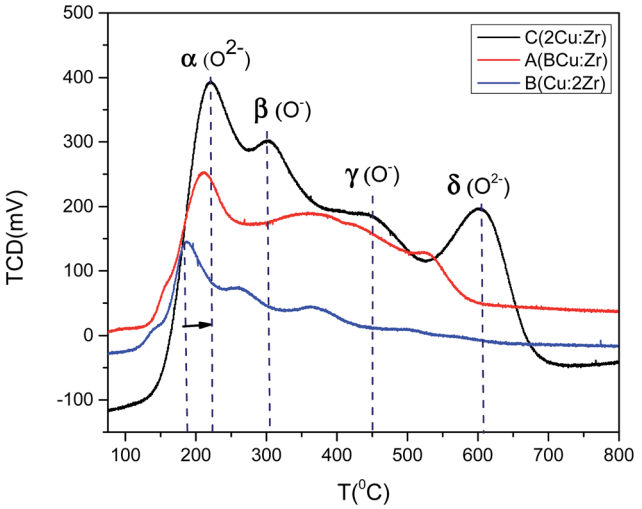

Fig. 10 O_2-TPD profile of catalyst A (Cu:Zr), catalyst B (Cu:2Zr), catalyst C (2Cu:Zr).

from oxygen vacancy sites on the catalyst's surface.[60] This oxidation step required low temperature to be reduced as they are weakly held at the sites. Moreover, the most intense shoulder peak of catalyst B (Cu:2Zr) implies a large concentration of desorbed surface oxygen species occurring at a low temperature and which thus enhanced the catalytic activity (Fig. 15). Moreover, the broad peak at higher temperature corresponds to reduction of lattice oxygen (O^{2-}). Moreover, the catalyst with a higher loading of Cu in the preparation protocol required large consumption of H_2 as reflected by peak broadening. In addition, the consistent shifting of the broad peaks towards high reduction temperatures in the order of catalyst B (Cu:2Zr) < A (Cu:Zr) < C (2Cu:Zr) indicated the magnitude of the interaction between Cu and ZrO_2 in the catalyst framework. Hence, it worthwhile to mention from the apparent shifting that the ratio of Cu to 2Zr in the bulk phase of the catalyst favored formation of the highest degree of a Cu–O–Zr phase. Consequently, this electronic interaction in the Cu–O–Zr phase induced improvement of the reducing capabilities of the catalyst at a low reduction temperature.

To further evaluate catalyst activation and O_2 desorption behavior, O_2-TPD was investigated (Fig. 10). We speculated that oxidation of the catalyst took place in four distinctive steps denoted by α, β, γ, and δ. The oxidation peak at the lower temperature around 180–210 °C was possibly due to the desorption of physiosorbed (O^{2-}) species at the present surface oxygen vacant sites as suggested by O 1s XPS spectra. Hence, the α peak in the TPD profile was attributed to O^{2-}. Oxygen desorption at (O^-) species occurred at comparatively higher temperatures (>400 °C) than O^{2-} species (<300 °C). So, it was reasonable to assign β and γ peaks to O^- species. The δ desorption peak could be attributed to the lattice oxygen species as it required a high temperature (>800 °C). It is worthwhile mentioning that the oxygen desorption peak at low temperature for catalyst B with high content of Zr was greatly shifted towards a lower temperature. That was indicative of enhancement of the oxygen mobility on the surface of the catalyst which facilitated the redox ability. This phenomenon could considerably enhance the catalytic activity observed for catalyst B (Fig. 15). In addition, the oxygen uptake at lower temperatures for catalyst B was greater (566 μmol g^{-1}) than catalyst C (522 μmol g^{-1}) and catalyst A (285 μmol g^{-1}). Based on the amount of oxygen desorption, we conclude that catalyst B contains the highest degree of physiosorbed (O^{2-}) species associated with surface defects at low temperature which notably improved the catalytic activity. Therefore, the oxygen adsorption occurs in the following sequence based on the O_2-TPD profile:

$$O_2(ad) \rightarrow O^{2-}(ad) \rightarrow O^-(ad) \rightarrow O^{2-}(lattice)$$

Catalytic activity

The catalyst $CuZrO_3$ (Cu:2Zr) was considered to optimize reaction parameters such as catalyst loading, time, temperature, and pressure in aerobic oxidation of vanillyl alcohol in base-free conditions. Acetonitrile was chosen as the solvent as it showed promising catalytic activity for other catalysts in an aerobic oxidation of vanillyl alcohol.[20] We prepared two other catalysts labeled as catalyst A (Cu:Zr) and catalyst C (2Cu:Zr) which were also experimented with at determined suitable reaction conditions. A blank reaction was also carried out without the presence of a catalyst and no conversion was observed. This implied that the oxidation reaction does not proceed in absence of a catalyst.

The progress of the reaction was recorded after every half an hour time interval until the reaction time reached 2.5 hours and the results are displayed in Fig. 11 (reaction conditions: 3 mmol vanillyl alcohol, 21 bar air pressure, 0.0025 g cm^{-3} catalyst B (Cu:2Zr), 120 °C). The catalytic activity was improved as expected at a precipitous rate with the increase of time until 2 hours of reaction time. The conversion was measured as 91% conversion with 76% selectivity with a reaction time of 2 h. Thereafter, the reaction progress was not significant as only enrichment of 2% in conversion was produced due to the

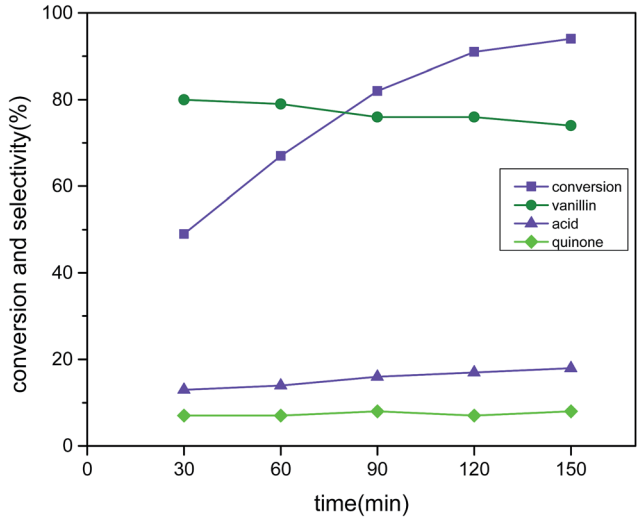

Fig. 11 Effect of time on conversion and selectivity in aerobic oxidation. Reaction conditions: 3 mmol vanillyl alcohol, 60 mL acetonitrile, 21 bar air pressure, 120 °C, catalyst mass (Cu:2Zr) 0.0025 g cm^{-3}.

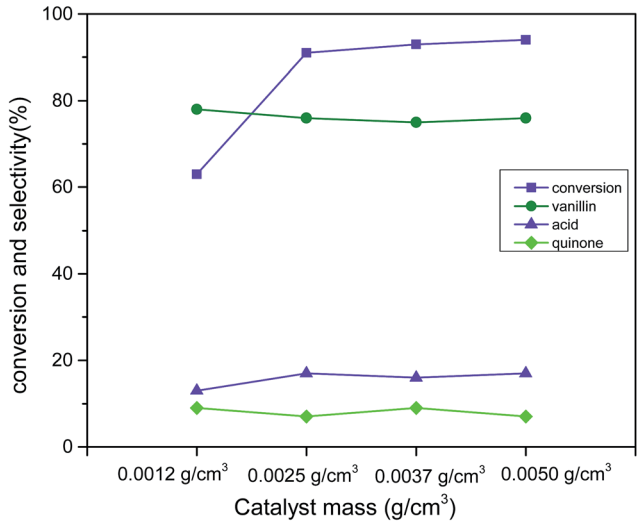

Fig. 12 Effect of catalyst loading (Cu:2Zr) on conversion and selectivity in aerobic oxidation. Reaction conditions: 3 mmol vanillyl alcohol, 60 mL acetonitrile, 21 bar air pressure, 120 °C, 2 h.

formation of 2-methoxy benzoquinone, which is a well-known radical trapping agent that can decrease the rate of reaction. Thus, 2 hours was chosen as the optimum reaction time. It is noteworthy that vanillic acid (17%) and quinone (7%) were found as the only detected side products by HPLC analysis. The perovskite type $CuZrO_3$ catalyst was outstanding for improving catalytic conversion by aerobic oxidation of vanillyl alcohol as compared with other previously reported literature references under short reaction times.[21,22]

To examine the obvious influence of catalyst loading, catalyst (Cu:2Zr) mass in a range 0.0012 g cm^{-3} to 0.0050 g cm^{-3} was considered (reaction conditions: 3 mmol vanillyl alcohol, 21 bar air pressure, 120 °C, 2 h) (Fig. 12). A steep improvement in the

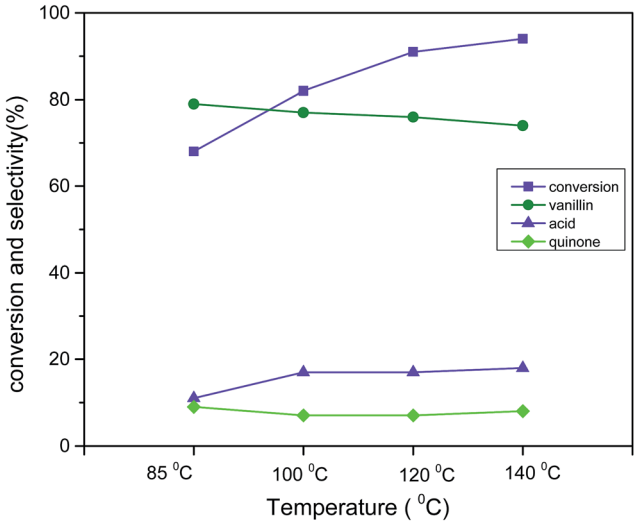

Fig. 13 Effect of temperature on conversion and selectivity in aerobic oxidation. Reaction conditions: 3 mmol vanillyl alcohol, 60 mL acetonitrile, 21 bar air pressure, catalyst mass (Cu:2Zr) 0.0025 g cm^{-3}, 2 h.

catalytic conversion to 91% from 63% was observed while the catalyst loading was changed to 0.0025 g cm^{-3} from 0.0012 g cm^{-3}. However, further increments in the catalyst loading up to 0.0050 g cm^{-3} was observed not to promote noticeable catalytic conversion. This was due to the earlier mentioned fact of mass transfer resistance.[61] Noteworthy, the selectivity (76%) was not affected by changes in the catalyst loading.

The apparent response in catalytic activity with respect to temperature was investigated in range of 85 °C to 140 °C (reaction condition: 3 mmol vanillyl alcohol, 21 bar air pressure, 0.0025 g cm^{-3} catalyst B (Cu:2Zr), 2 h) (Fig. 13). The catalytic conversion was substantially improved to 94% from 68% when the temperature was elevated from 85 °C to 140 °C. However, the selectivity slightly decreased by 5% from the initial selectivity

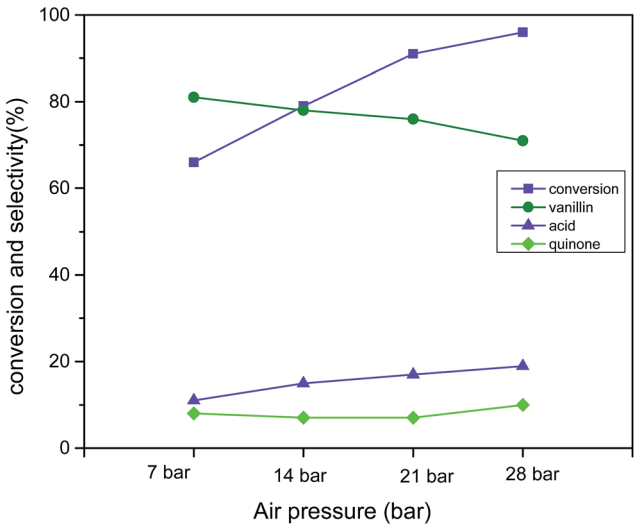

Fig. 14 Effect of air pressure on conversion and selectivity in aerobic oxidation. Reaction conditions: 3 mmol vanillyl alcohol, 60 mL acetonitrile, 120 °C, catalyst mass (Cu:2Zr) 0.0025 g cm^{-3}, 2 h.

(79%) with that increment of temperature. This was possibly due to next step-oxidation of the product vanillin to its corresponding acid at higher temperatures. It was worthwhile mentioning that char formation was observed at the high temperature 140 °C. Therefore, 120 °C was considered the best temperature for liquid phase aerobic oxidation of vanillyl alcohol. The obtained reaction temperature 120 °C with 91% conversion was comparatively lower than in other reports.[20] This clearly evidenced that a perovskite type $CuZrO_3$ catalyst prepared *via* the solvent evaporation technique was superior in terms of catalytic activity at mild reaction conditions.

Air pressure was found to be the vital determinant to obtain superior catalytic activity from 7 bar to 28 bar (reaction condition: 3 mmol vanillyl alcohol, 0.0025 g cm^{-3} catalyst B (Cu:2Zr), 120 °C, 2 h) (Fig. 14). The pressure was changed from 7 bar to 14 bar, and the conversion was enriched to 79% from 66%, but a drop in the selectivity to 78% from 81% resulted for vanillin. When the pressure was increased to 21 bar air pressure, excellent catalytic activity was measured at 91% conversion with 76% selectivity to vanillin. Further rise in the air pressure was found to be detrimental to the selectivity (71%) but to the contrary, conversion was further improved up to 96%. The slight drop in the selectivity was associated with the over-oxidation of vanillin to vanillic acid in presence of excess desorbed oxygen in the solvent. Based on the experimental data, 21 bar air pressure was selected as the optimum pressure for liquid phase aerobic oxidation of vanillyl alcohol.

The prepared catalysts A (Cu:Zr), B (Cu:2Zr), and C (2Cu:Zr) were tested for oxidation of vanillyl alcohol at the obtained reaction conditions (Fig. 15). To rationalize, commercially available pure CuO, ZrO_2, and catalyst (Cu:2Zr) prepared without TFA were also used as catalysts at the same conditions as catalyst B (Cu:2Zr). Isolated CuO catalyst showed 4% conversion with 72% selectivity and 6% conversion with 68% selectivity for ZrO_2. And, catalysts synthesized without the addition of trifluoroacetic acid showed catalytic conversion of 41% with 71% selectivity. Interestingly, the synthesized catalysts showed more improved catalytic action than their counterpart single oxide catalysts. For catalyst A (Cu:Zr), conversion (67%) with selectivity (75%) was achieved. When catalyst B (Cu:2Zr) was used, the best conversion (91%) with selectivity (76%) was obtained. The least conversion (43%) with selectivity (76%) was observed in the case of catalyst C (2Cu:Zr). It is worth noting that the selectivity towards vanillin in the case of all prepared catalysts was almost the same because the same XRD fingerprint was identified in the catalysts with different ratios. Comparison of catalytic activity of synthesized catalyst B (Cu:2Zr) with and without TFA indicated that introduction of TFA in the synthesis step induced formation of more surface oxygen vacancies as evident in O 1s XPS spectra and O_2-TPD. Thus, catalytic conversion was substantially enriched when the surface oxygen vacant sites were present in large concentrations on the catalyst. Surface oxygen vacant sites could hold various weakly bonded oxygen species on the surface which could possibly accelerate oxygen mobility from the catalyst surface to substrate. It is worth mentioning that the highest catalytic activity was obtained by catalyst B (Cu:Zr) and was due to the high content of ZrO_2. High loading of ZrO_2 could cause a large concentration of acidic sites on the surface to strongly interact with Cu^{2+} ion on the surface. Consequently, formation of a high degree of Cu–O–Zr active phase occurred in the catalyst and it was presumed that Cu–O–Zr was the active phase for oxidation of vanillyl alcohol. The catalytic activity of synthesized $CuZrO_3$ catalyst could be due to presence of Cu^{+}/Cu^{2+} and Zr^{3+}/Zr^{4+} ion pairs generated by one electron transfer between these ions during O_2 activation. These ions could form a metal superoxo intermediate (M–O–O·) reactive species by oxygen reduction on the catalyst for the selective oxidation of alcohol.[62] Also, high dispersion of Cu on the ZrO_2 in catalyst B (Cu:2Zr) minimizes the grain size to less than 10 nm and exposed numerous grain boundaries which were observed in the HRTEM micrograph (Fig. 6e). Furthermore, the order of catalytic performance (Cu:2Zr > Cu:Zr > 2Cu:Zr) was in good agreement with that of the above-

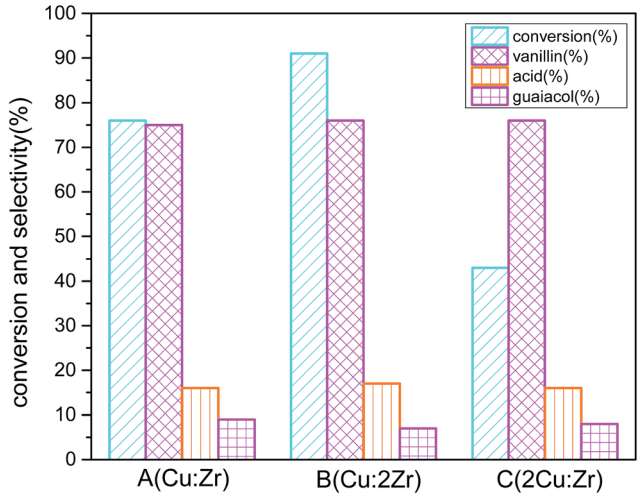

Fig. 15 Effect of catalyst composition on conversion and selectivity in aerobic oxidation. Reaction conditions: 3 mmol vanillyl alcohol, 21 bar air pressure, 60 mL acetonitrile, 120 °C, catalyst mass 0.0025 g cm^{-3}, 2 h.

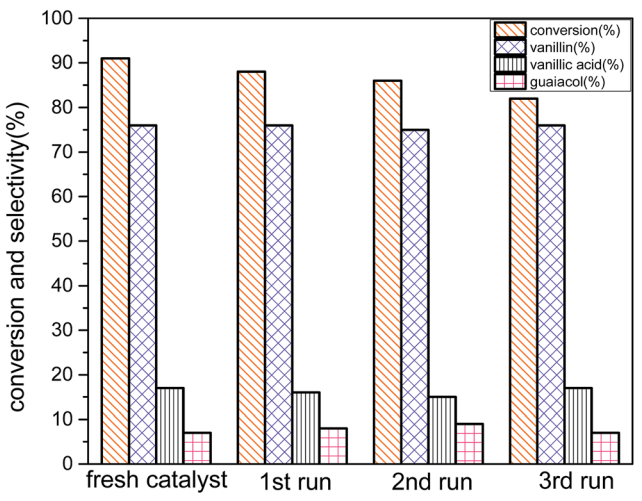

Fig. 16 Recycling study on conversion and selectivity in aerobic oxidation. Reaction conditions: 3 mmol vanillyl alcohol, 21 bar air pressure, 60 mL acetonitrile, 120 °C, catalyst mass (Cu:2Zr) 0.0025 g cm^{-3}, 2 h.

Table 4 Comparison of current preparation methods with available methods in literatures for Cu–Zr mixed oxide

Methods	Applications	Problems of available methods	Advantages of current method
Sol–gel nanocasting	Steam reforming of methanol	Complicated Multiple steps	One pot Facile
Co-precipitation	Partial oxidation of methane	Separate phase Low reducing ability	Superior crystallinity Small crystallite size
Chemical vapor deposition	Methanol oxidation	Thin films Low catalytic activity	Homogeneity of metals
Current method (solvent evaporation)	Vanillyl alcohol oxidation		High catalytic activity Stable phase

mentioned BET surface area as a large surface area could offer exposure to many active sites to partake in the reaction.

Stability of the catalyst was also examined using the reused catalyst for oxidation of vanillyl alcohol at the optimum reaction conditions (reaction conditions: 3 mmol vanillyl alcohol, 0.0025 g cm^{-3} catalyst B (Cu:2Zr), 21 bar air pressure, 85 °C, 4 h) (Fig. 16). After catalytic reaction, the catalyst was recovered by filtration and washed several times with acetonitrile to remove desorbed oxygenated products on the surface. The spent catalyst was dried at 80 °C for 4 hours. The subsequent reactions were carried out at the optimum reaction conditions following the similar recovery procedure. There was a slight loss of the catalytic activity in the recycled catalysts. However, the selectivity remained almost unchanged at 76% for all consecutive reactions. That indicated that similar reaction pathways were governed with all recycling experiments. Crystal phase was well preserved as in the fresh catalyst during a recycling procedure, so there was no obvious change in the amount of selectivity. But, the amount of conversion was decreased possibly owing to transformation of uneven surface to a plain surface after the catalytic reaction (Fig. 5d) and blockage on the active sites by un-desorbed oxygenated products.

Moreover, a leaching test was also conducted using ICP-MS analysis to investigate any leaching of metal ions into the reaction. Prior to starting the reaction, 0.5 dm^3 reaction mixture was collected and the same procedure was followed after completing the reaction. The results indicated that there was no significant change (<0.01 ppm) in the presence of metal ions in the reaction mixture after the catalytic reaction; this suggested that there was no leeching of metal ions in the reaction. In summary, the one pot solvent evaporation technique was compared with other available techniques for preparation of Cu–Zr mixed oxides in Table 4.[63–65]

Conclusion

A simple and facile solvent evaporation method was effective for preparing a highly crystalline and mesoporous $CuZrO_3$ nanoparticle catalyst with promising catalytic activity in liquid phase oxidation of vanillyl alcohol. The catalyst possessed a great amount of surface oxygen vacancies which improved the catalytic activity as testified by O 1s spectra and O_2-TPD analysis. Moreover, higher loading of ZrO_2 in the bulk phase of the catalyst contributed to formation of a large concentration Cu–O–Zr linkage as an active phase by the highest interaction of Cu with the ZrO_2 lattice thus leading to the improved redox property of the catalyst in a H_2-TPR profile. The highest catalytic activity was measured at 91% conversion and 76% selectivity to vanillin for catalyst $CuZrO_3$ (Cu:2Zr) in liquid phase aerobic oxidation of vanillyl alcohol under mild reaction conditions.

Acknowledgements

The authors are cordially grateful to Universiti Malaya grant GC001A-14AET for their financial support to accomplish this work. Also, the authors would like to thank Emy Marlina Samsudin for assistance in analysis of Raman spectrum.

References

1 C. Xu, R. A. D. Arancon, J. Labidi and R. Luque, *Chem. Soc. Rev.*, 2014, **43**, 7485–7500.
2 A. Halilu, T. H. Ali, A. Y. Atta, P. Sudarsanam, S. K. Bhargava and S. B. Abd Hamid, *Energy Fuels*, 2016, **30**, 2216–2226.
3 L. Hu, G. Zhao, W. Hao, X. Tang, Y. Sun, L. Lin and S. Liu, *RSC Adv.*, 2012, **2**, 11184–11206.
4 J. N. Chheda, G. W. Huber and J. A. Dumesic, *Angew. Chem., Int. Ed.*, 2007, **46**, 7164–7183.
5 V. Nair and R. Vinu, *J. Anal. Appl. Pyrolysis*, 2016, **119**, 31–39.
6 S. K. Hanson and R. T. Baker, *Acc. Chem. Res.*, 2015, **48**, 2037–2048.
7 P. J. Deuss and K. Barta, *Coord. Chem. Rev.*, 2016, **306**, 510–532.
8 P. T. Patil, U. Armbruster, M. Richter and A. Martin, *Energy Fuels*, 2011, **25**, 4713–4722.
9 M. Shilpy, M. A. Ehsan, T. H. Ali, S. B. A. Hamid and M. E. Ali, *RSC Adv.*, 2015, **5**, 79644–79653.
10 J. Pan, J. Fu and X. Lu, *Energy Fuels*, 2015, **29**, 4503–4509.
11 S. Saha and S. B. A. Hamid, *RSC Adv.*, 2016, **6**, 96314–96326.
12 S. Saha, S. B. A. Hamid and T. H. Ali, *Appl. Surf. Sci.*, 2017, **394**, 205–218.
13 R. Behling, S. Valange and G. Chatel, *Green Chem.*, 2016, **18**, 1839–1854.
14 H. Priefert, J. Rabenhorst and A. Steinbüchel, *Appl. Microbiol. Biotechnol.*, 2001, **56**, 296–314.
15 G. Ravishankar, B. Suresh, P. Giridhar, S. R. Rao and T. S. Johnson, *Capsicum: The genus Capsicum*, 2003, pp. 96–128.

16 R. Ma, Y. Xu and X. Zhang, *ChemSusChem*, 2015, **8**, 24–51.
17 G. Chatel and R. D. Rogers, *ACS Sustainable Chem. Eng.*, 2013, **2**, 322–339.
18 A. Jha and C. V. Rode, *New J. Chem.*, 2013, **37**, 2669–2674.
19 A. Jha, K. R. Patil and C. V. Rode, *ChemPlusChem*, 2013, **78**, 1384–1392.
20 A. Jha, D. Mhamane, A. Suryawanshi, S. M. Joshi, P. Shaikh, N. Biradar, S. Ogale and C. V. Rode, *Catal. Sci. Technol.*, 2014, **4**, 1771–1778.
21 P. B. Bhat and B. R. Bhat, *New J. Chem.*, 2015, **39**, 273–278.
22 L. Geng, M. Zhang, W. Zhang, M. Jia, W. Yan and G. Liu, *Catal. Sci. Technol.*, 2015, **5**, 3097–3102.
23 M. B. Gawande, R. K. Pandey and R. V. Jayaram, *Catal. Sci. Technol.*, 2012, **2**, 1113–1125.
24 D. A. Aguilera, A. Perez, R. Molina and S. Moreno, *Appl. Catal., B*, 2011, **104**, 144–150.
25 M. R. Morales, B. P. Barbero, T. Lopez, A. Moreno and L. E. Cadús, *Fuel*, 2009, **88**, 2122–2129.
26 W. Li, M. Zhuang and J. Wang, *Catal. Today*, 2008, **137**, 340–344.
27 J. Zhu and Q. Gao, *Microporous Mesoporous Mater.*, 2009, **124**, 144–152.
28 R. J. Voorhoeve, J. Remeika, P. Freeland and B. Matthias, *Science*, 1972, **177**, 353–354.
29 R. Voorhoeve, J. P. Remeika and D. Johnson, *Science*, 1973, **180**, 62–64.
30 R. Voorhoeve, J. Remeika and L. Trimble, *Mater. Res. Bull.*, 1974, **9**, 1393–1404.
31 R. Voorhoeve, L. Trimble and C. Khattak, *Mater. Res. Bull.*, 1974, **9**, 655–666.
32 P. Gallagher, D. Johnson and F. Schrey, *Mater. Res. Bull.*, 1974, **9**, 1345–1352.
33 K. Tabata and M. Misono, *Catal. Today*, 1990, **8**, 249–261.
34 N. Guilhaume and M. Primet, *J. Catal.*, 1997, **165**, 197–204.
35 H. Tanaka, *Catal. Surv. Asia*, 2005, **9**, 63–74.
36 S. Keav, S. K. Matam, D. Ferri and A. Weidenkaff, *Catalysts*, 2014, **4**, 226–255.
37 R. Voorhoeve, J. Remeika and L. Trimble, *Ann. N. Y. Acad. Sci.*, 1976, **272**, 3–21.
38 M. Islam, M. Cherry and L. Winch, *J. Chem. Soc., Faraday Trans.*, 1996, **92**, 479–482.
39 Y. Teraoka, H.-M. Zhang and N. Yamazoe, *Chem. Lett.*, 1985, **14**, 1367–1370.
40 Z. Yu, L. Gao, S. Yuan and Y. Wu, *J. Chem. Soc., Faraday Trans.*, 1992, **88**, 3245–3249.
41 M. O'Connell, A. Norman, C. Hüttermann and M. Morris, *Catal. Today*, 1999, **47**, 123–132.
42 Y. Teraoka, M. Yoshimatsu, N. Yamazoe and T. Seiyama, *Chem. Lett.*, 1984, **13**, 893–896.
43 E. M. Samsudin, S. B. A. Hamid, J. C. Juan, W. J. Basirun, A. E. Kandjani and S. K. Bhargava, *Appl. Surf. Sci.*, 2016, **365**, 57–68.
44 M. A. Ehsan, H. Khaledi, Z. Arifin and M. Mazhar, *Polyhedron*, 2015, **98**, 190–195.
45 A. Reller and T. Williams, *Chem. Br.*, 1989, **25**, 1227–1230.
46 M. Li, Z. Feng, P. Ying, Q. Xin and C. Li, *Phys. Chem. Chem. Phys.*, 2003, **5**, 5326–5332.
47 H. Hagemann, H. Bill, E. Walker and M. François, *Solid State Commun.*, 1990, **73**, 447–451.
48 C. Perry, D. W. Liu and R. P. Ingel, *J. Am. Ceram. Soc.*, 1985, **68**, C-184–C-187.
49 H. Tanaka and M. Misono, *Curr. Opin. Solid State Mater. Sci.*, 2001, **5**, 381–387.
50 L. Wang, J. Teng, P. Liu, A. Hirata, E. Ma, Z. Zhang, M. Chen and X. Han, *Nat. Commun.*, 2014, **5**, 4402.
51 S. Royer, D. Duprez and S. Kaliaguine, *J. Catal.*, 2005, **234**, 364–375.
52 J.-G. Choi, J. R. Brenner, C. W. Colling, B. G. Demczyk, J. L. Dunning and L. T. Thompson, *Catal. Today*, 1992, **15**, 201–222.
53 R. Vidruk, M. V. Landau, M. Herskowitz, M. Talianker, N. Frage, V. Ezersky and N. Froumin, *J. Catal.*, 2009, **263**, 196–204.
54 W. Choo and J. Y. Lee, *Metall. Trans. A*, 1982, **13**, 135–140.
55 J. Wang, T. J. Shi and X. Jiang, *Nanoscale Res. Lett.*, 2009, **4**, 240–246.
56 I.-H. Tseng, J. C. Wu and H.-Y. Chou, *J. Catal.*, 2004, **221**, 432–440.
57 T. Mathew, N. Shiju, K. Sreekumar, B. S. Rao and C. S. Gopinath, *J. Catal.*, 2002, **210**, 405–417.
58 M. Roberts, *Chem. Soc. Rev.*, 1989, **18**, 451–475.
59 H. Deng, L. Lin and S. Liu, *Energy Fuels*, 2010, **24**, 4797–4802.
60 T. Nitadori, T. Ichiki and M. Misono, *Bull. Chem. Soc. Jpn.*, 1988, **61**, 621–626.
61 R. Klaewkla, M. Arend and W. F. Hoelderich, *A review of mass transfer controlling the reaction rate in heterogeneous catalytic systems*, INTECH Open Access Publisher, 2011.
62 I. Fernández, J. R. Pedro, A. L. Roselló, R. Ruiz, I. Castro, X. Ottenwaelder and Y. Journaux, *Eur. J. Org. Chem.*, 2001, **2001**, 1235–1247.
63 H. Purnama, F. Girgsdies, T. Ressler, J. H. Schattka, R. A. Caruso, R. Schomäcker and R. Schlögl, *Catal. Lett.*, 2004, **94**, 61–68.
64 M. Schmal, C. A. Perez, V. T. da Silva and L. F. Padilha, *Appl. Catal., A*, 2010, **375**, 205–212.
65 M. A. Ehsan, A. S. Hakeem, H. Khaledi, M. Mazhar, M. M. Shahid, A. Pandikumar and N. M. Huang, *RSC Adv.*, 2015, **5**, 103852–103862.